

Image Segmentation by Image Foresting Transform with Non-smooth Connectivity Functions

Lucy A. C. Mansilla*, Paulo A. V. Miranda

Department of Computer Science,
University of São Paulo (USP),
05508-090, São Paulo, SP, Brazil.

Email: lucyacam@vision.ime.usp.br, pmiranda@vision.ime.usp.br

Abstract—Image segmentation, such as to extract an object from a background, is very useful for medical and biological image analysis. In this work, we propose new methods for interactive segmentation of multidimensional images, based on the Image Foresting Transform (IFT), by exploiting for the first time non-smooth connectivity functions (NSCF) with a strong theoretical background. The new algorithms provide global optimum solutions according to an energy function of graph cut, subject to high-level boundary constraints (polarity and shape), or consist in a sequence of paths’ optimization in residual graphs.

Our experimental results indicate substantial improvements in accuracy in relation to other state-of-the-art methods, by allowing the customization of the segmentation to a given target object.

Keywords—graph cut; image foresting transform; oriented image foresting transform; non-smooth connectivity function; geodesic star convexity;

I. INTRODUCTION

Image segmentation is one of the most fundamental and challenging problems in image processing and computer vision [2]. In medical image analysis, accurate segmentation results commonly require the user intervention because of the presence of structures with ill-defined borders, intensity non-standardness among images, field inhomogeneity, noise, artifacts, partial volume effects, and their interplay [3]. The high-level, application-domain-specific knowledge of the user is also often required in the digital matting of natural scenes, because of their heterogeneous nature [4]. These problems motivated the development of several methods for semi-automatic segmentation [5], [6], [7], aiming to minimize the user involvement and time required without compromising accuracy and precision.

One important class of interactive image segmentation comprises seed-based methods, which have been developed based on different theories, supposedly not related, leading to different frameworks, such as *watershed from markers* [7], *random walks* [8], *fuzzy connectedness* [9], *graph cuts* [6], *distance cut* [4], *image foresting transform* (IFT) [10], and *grow cut* [11]. The study of the relations among different frameworks, including theoretical and empirical comparisons, has a vast literature [12], [13], [14]. However, these methods in most studies are restricted to undirected graphs, and the most time-efficient methods, including the IFT, present a lack

of boundary regularization constraints. Moreover, the quality of their segmentation results with minimal user intervention, strongly depends on an adequate estimate of the weights assigned to the graph’s arcs [15].

The main contribution of this work is a theoretical development to support the usage of *non-smooth connectivity functions* (NSCF) in the IFT, opening new perspectives in the research of image processing using graphs, since NSCF were, until now, avoided in the literature. More specifically, we prove that some NSCF can lead to optimum results according to a graph-cut measure on a digraph [16], [17] or consist in a sequence of paths’ optimization in residual graphs. We have as main results:

- 1) The customization of the segmentation by IFT to match the global and local features of a target object: **(a)** The design of more adaptive and flexible connectivity functions, which allow better handling of images with strong inhomogeneity by using dynamic weights. **(b)** The orientation of the object’s intensity transitions, i.e., bright to dark or the opposite (boundary polarity), and **(c)** shape constraints to regularize the segmentation boundary (geodesic star convexity constraint).
- 2) The development of an interactive segmentation tool within the software, called *Brain Image Analyzer* (BIA), to support research in neurology involving volumetric magnetic resonance images of a 3T scanner from the FAPESP-CInApCe.
- 3) Four conference papers were published in international events of high regard [17], [18], [19], [20], and one journal paper was published in the *IEEE Transactions on Image Processing* (impact factor: 3.111) [16].

For the sake of completeness in presentation, Section II includes the relevant previous work of image segmentation by IFT. In Sections III, IV, V and VI, we present the main contributions covered in the master’s dissertation [1]: The classification of NSCF, the use of adaptive weights via NSCF, the boundary polarity through digraphs, and the elimination of false delineations by shape constraints. Our conclusions are stated in Section VII.

II. IMAGE FORESTING TRANSFORM (IFT)

An image 2D/3D can be interpreted as a weighted digraph $G = \langle \mathcal{V} = \mathcal{I}, \xi, \omega \rangle$ whose nodes \mathcal{V} are the image pixels in its

* This work relates to the M.Sc. dissertation [1].

image domain $\mathcal{I} \subset \mathbb{Z}^N$, and whose arcs are the ordered pixel pairs $(s, t) \in \xi$ (e.g., 4-neighborhood, or 8-neighborhood, in case of 2D images, and 6-neighbors in 3D). The digraph G is symmetric if for any of its arcs (s, t) , the pair (t, s) is also an arc of G . We have an undirected graph when $\omega(s, t) = \omega(t, s)$ in a symmetric graph G . We use $(s, t) \in \xi$ or $t \in \xi(s)$ to indicate that t is adjacent to s . Each arc $(s, t) \in \xi$ may have a weight $\omega(s, t) \geq 0$, such as a dissimilarity measure between pixels s and t (e.g., $\omega(s, t) = |I(t) - I(s)|$ for a single channel image with values given by $I(t)$).

For a given image graph G , a path $\pi_t = \langle t_1, t_2, \dots, t_n = t \rangle$ is a sequence of adjacent pixels with terminus at a pixel t . A path is *trivial* when $\pi_t = \langle t \rangle$. A path $\pi_t = \pi_s \cdot \langle s, t \rangle$ indicates the extension of a path π_s by an arc (s, t) . The notation $\pi_{s \rightsquigarrow t} = \langle t_1 = s, t_2, \dots, t_n = t \rangle$ may also be used, where s stands for the origin and t for the destination node. A *predecessor map* is a function P that assigns to each pixel t in \mathcal{V} either some other adjacent pixel in \mathcal{V} , or a distinctive marker *nil* not in \mathcal{V} — in which case t is said to be a *root* of the map. A *spanning forest* is a predecessor map which contains no cycles — i.e., one which takes every pixel to *nil* in a finite number of iterations. For any pixel $t \in \mathcal{V}$, a spanning forest P defines a path π_t^P recursively as $\langle t \rangle$ if $P(t) = \text{nil}$, and $\pi_s^P \cdot \langle s, t \rangle$ if $P(t) = s \neq \text{nil}$.

A *connectivity function* computes a value $f(\pi_t)$ for any path π_t , usually based on arc weights. A path π_t is *optimum* if $f(\pi_t) \leq f(\tau_t)$ for any other path τ_t in G . By taking to each pixel $t \in \mathcal{V}$ one optimum path with terminus t , we obtain the optimum-path value $V(t)$, which is uniquely defined by $V(t) = \min_{\forall \pi_t \text{ in } G} \{f(\pi_t)\}$. A path $\pi_{t_n} = \langle t_1, t_2, \dots, t_n \rangle$ is *complete optimum* if all paths $\pi_{t_i} = \langle t_1, t_2, \dots, t_i \rangle$, $i = 1, 2, \dots, n$ are optimum paths. The IFT takes an image graph G , and a path-cost function f ; and assigns one optimum path π_t to every pixel $t \in \mathcal{V}$ such that an *optimum-path forest* P is obtained — i.e., a spanning forest where all paths are optimum. However, f must be *smooth* (Definition 1), otherwise, the paths may not be optimum [10].

Definition 1 (Smooth path-cost function). *A path-cost function f is smooth if for any pixel $t \in \mathcal{I}$, there is an optimum path π_t , which either is trivial, or has the form $\pi_s \cdot \langle s, t \rangle$ where*

- (C1) $f(\pi_s) \leq f(\pi_t)$,
- (C2) π_s is optimum, and
- (C3) for any optimum path π'_s ending at s , $f(\pi'_s \cdot \langle s, t \rangle) = f(\pi_t)$.

We consider image segmentation from two seed sets, \mathcal{S}_o and \mathcal{S}_b ($\mathcal{S}_o \cap \mathcal{S}_b = \emptyset$), containing pixels selected inside and outside the object, respectively. The search for optimum paths is constrained to start in $\mathcal{S} = \mathcal{S}_o \cup \mathcal{S}_b$. The image is partitioned into two optimum-path forests — one rooted at the internal seeds, defining the object, and the other rooted at the external seeds, representing the background. A label, $L(t) = 1$ for all $t \in \mathcal{S}_o$ and $L(t) = 0$ for all $t \in \mathcal{S}_b$, is propagated to all unlabeled pixels during the computation [10].

III. IFT WITH NON-SMOOTH CONNECTIVITY FUNCTIONS

Clearly, from Definition 1, we have that a connectivity function is not smooth if it doesn't satisfy at least one of the conditions C1, C2 or C3. For example $f_{\sum|\Delta I|}$ violates C2 and C3:

$$f_{\sum|\Delta I|}(\langle t \rangle) = \begin{cases} 0, & \text{if } t \in \mathcal{S}, \\ +\infty, & \text{otherwise.} \end{cases} \quad (1)$$

$$f_{\sum|\Delta I|}(\pi_{r \rightsquigarrow s} \cdot \langle s, t \rangle) = f_{\sum|\Delta I|}(\pi_{r \rightsquigarrow s}) + |I(t) - I(r)|$$

In [20], we formally classified several non-smooth functions (Figure 1) according to the conditions C1, C2 and C3 (Definition 1), and C4 (Definition 2).

Definition 2 (Condition C4). *A path-value function f satisfies the condition C4, if for any node $s \in \mathcal{I}$ the following condition is verified $\forall t \in \xi(s)$:*

- For any paths π_s and π'_s ending at s , if $f(\pi_s) = f(\pi'_s)$, then we have $f(\pi_s \cdot \langle s, t \rangle) = f(\pi'_s \cdot \langle s, t \rangle)$.

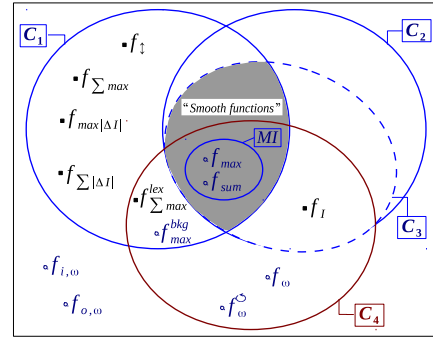


Fig. 1. Schematic representation of the relations between smooth and non-smooth connectivity functions: C_1 , C_2 , C_3 , and C_4 are sets of connectivity functions that satisfy these respective conditions for a general graph.

IV. ADAPTIVE WEIGHTS VIA NSCF

Methods based on IFT [10] have been successfully used in the segmentation of 1.5 Tesla MR datasets [21], [22]. However, inhomogeneity effects are stronger in higher magnetic fields, and it is extremely important to define the optimal solution for these images. NSCFs are more adaptive to cope with the problems of field inhomogeneity, which are common in MR images of 3 Tesla [23].

In order to give a theoretical foundation to support the usage of NSCF, we theoretically proved that the IFT with any non-smooth function $f \in (C_1 \cap C_4) \setminus C_2$ is, in fact, equivalent to the result of a sequence of optimizations, each of them involving a maximal set of elements, in a well-structured way [20]. This proof was supported by the following proposition:

Proposition 1. *Consider a function $f \in (C_1 \cap C_4) \setminus C_2$. For a given image graph $G = \langle \mathcal{V}, \xi, \omega \rangle$, and set of seeds \mathcal{S} , let \mathcal{O} be the set of all pixels $t \in \mathcal{V}$, such that there exists a complete-optimum path π_t for f . In any spanning forest P computed in G by the IFT algorithm for f , all the paths τ_t^P with $t \in \mathcal{O}$ are optimum paths.*

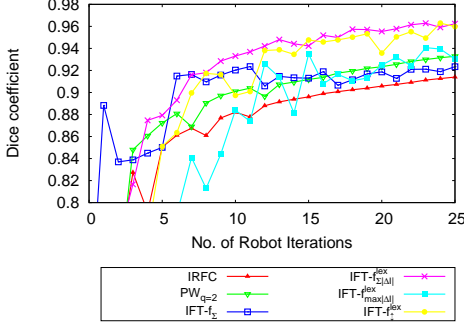


Fig. 2. Results using a robot user for segmenting the 3D brain dataset.

In our experiments, we used 10 T1-weighted 3D images of male and female adults with normal brains. The image dataset included the head and, at least, a small portion of the neck. Our experimental result, using a robot user¹ for segmenting the brain dataset, indicates that substantial improvements can be obtained by NSCFs in the 3D segmentation of MR images of 3 Tesla, with strong inhomogeneity effects, when compared to smooth connectivity functions. That is because NSCFs permit a more adaptive configuration of the arc weights.

Figure 2 shows the experimental curves, where *IRFC* [9] and $PW_{q=2}$ [14] represent different algorithms related to the smooth function f_{\max} , and we used $\omega(s, t) = G(s) + G(t)$, where $G(s)$ is the magnitude of Sobel gradient at a voxel s . Clearly, $f_{\sum|\Delta I|}^{lex}$ presented the best accuracy. Figure 3 shows one example for user-selected markers. These results emphasize the importance of non-smooth connectivity functions. The non-smooth connectivity function $f_{\sum|\Delta I|}^{lex}$ is a variation of $f_{\sum|\Delta I|}$ (Eq. 1), in order to guarantee that $f_{\sum|\Delta I|}^{lex} \in (\mathcal{C}_1 \cap \mathcal{C}_4) \setminus \mathcal{C}_2$ [20]. The function $f_{\sum|\Delta I|}^{lex}$ gives pairs of values that should be compared according to the lexicographical order. The first component is the non-smooth function $f_{\sum|\Delta I|}$ (Eq. 1), and the second is the priority level of the seed/root for that path. The lower its value the higher is its priority. In interactive segmentation, we give lower priority for new inserted seeds, since they are used mainly for corrective actions, so that we can keep their effects more locally. The same process was done for $f_{\max|\Delta I|}^{lex} \in (\mathcal{C}_1 \cap \mathcal{C}_4) \setminus \mathcal{C}_2$ and $f_{\downarrow}^{lex} \in (\mathcal{C}_1 \cap \mathcal{C}_4) \setminus \mathcal{C}_2$, in relation to $f_{\max|\Delta I|}$ and f_{\downarrow} , respectively [20].

V. BOUNDARY POLARITY VIA NSCF

In order to resolve between very similar nearby boundary segments, in [16], [17] we successfully incorporated the boundary polarity constraint in the IFT using NSCF in digraphs, resulting in a novel method called **Oriented Image Foresting Transform** (OIFT).

In the case of digraphs, there are two different types of cut for each object boundary: an inner-cut boundary composed by arcs that point toward object pixels

¹Method introduced in [24], to simulate user interaction of interactive segmentation.

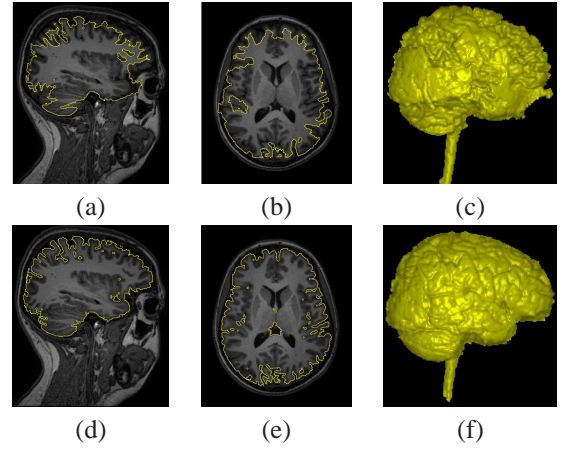


Fig. 3. Brain segmentation results for the same user-selected markers by (a-c) f_{\max} , and (d-f) $f_{\sum|\Delta I|}^{lex}$.

$\mathcal{C}_i(L) = \{(s, t) \in \xi \mid L(s) = 0, L(t) = 1\}$, and an outer-cut boundary with arcs from object to background pixels $\mathcal{C}_o(L) = \{(s, t) \in \xi \mid L(s) = 1, L(t) = 0\}$. Consequently, we consider two different types of energy, E_i (Eq. 2) and E_o (Eq.3).

$$E_i(L, G) = \min_{(s, t) \in \mathcal{C}_i(L)} \omega(s, t) \quad (2)$$

$$E_o(L, G) = \min_{(s, t) \in \mathcal{C}_o(L)} \omega(s, t) \quad (3)$$

We use a digraph, where $\omega(s, t)$ is a combination of a regular undirected dissimilarity measure $\psi(s, t)$, multiplied by an orientation factor (i.e., $\omega(s, t) = \psi(s, t) \times (1 + \alpha)$ if $I(s) > I(t)$ and $\omega(s, t) = \psi(s, t) \times (1 - \alpha)$ otherwise). Several different procedures can be adopted for $\psi(s, t)$, such as the absolute value of the difference of image intensities (i.e., $\psi(s, t) = |I(t) - I(s)|$). Note that we have $\omega(s, t) \neq \omega(t, s)$ when $\alpha > 0$.

The OIFT is build upon the IFT framework by considering one of the following path functions in a symmetric digraph:

$$\begin{aligned} f_{\max}^{\mathcal{S}_1, \mathcal{S}_2}(\langle t \rangle) &= \begin{cases} -1 & \text{if } t \in \mathcal{S}_1 \cup \mathcal{S}_2 \\ +\infty & \text{otherwise} \end{cases} \\ f_{\max}^{\mathcal{S}_1, \mathcal{S}_2}(\pi_{r \rightsquigarrow s} \cdot \langle s, t \rangle) &= \begin{cases} Expr1 & \text{if } r \in \mathcal{S}_1 \\ Expr2 & \text{if } r \in \mathcal{S}_2 \end{cases} \\ Expr1 &= \max\{f_{\max}^{\mathcal{S}_1, \mathcal{S}_2}(\pi_{r \rightsquigarrow s}), 2 \times \omega(t, s) + 1\} \\ Expr2 &= \max\{f_{\max}^{\mathcal{S}_1, \mathcal{S}_2}(\pi_{r \rightsquigarrow s}), 2 \times \omega(s, t)\} \\ f_{\omega}^{\mathcal{S}_1, \mathcal{S}_2}(\langle t \rangle) &= f_{\max}^{\mathcal{S}_1, \mathcal{S}_2}(\langle t \rangle) \\ f_{\omega}^{\mathcal{S}_1, \mathcal{S}_2}(\pi_{r \rightsquigarrow s} \cdot \langle s, t \rangle) &= \begin{cases} \omega(t, s) & \text{if } r \in \mathcal{S}_1 \\ \omega(s, t) & \text{if } r \in \mathcal{S}_2 \end{cases} \end{aligned} \quad (4)$$

The segmentation using $f_{\max}^{\mathcal{S}_o, \mathcal{S}_b}$ or $f_{\omega}^{\mathcal{S}_o, \mathcal{S}_b}$ favors transitions from dark to bright pixels, and $f_{\max}^{\mathcal{S}_b, \mathcal{S}_o}$ or $f_{\omega}^{\mathcal{S}_b, \mathcal{S}_o}$ favors the opposite orientation, according to Theorem 1. In the case of multiple candidate segmentations with the same energy, $f_{\omega}^{\mathcal{S}_1, \mathcal{S}_2}$ produces a better handling of the tie zones than $f_{\max}^{\mathcal{S}_1, \mathcal{S}_2}$ [17].

Theorem 1 (Inner/outer-cut boundary optimality). *For two given sets of seeds \mathcal{S}_o and \mathcal{S}_b , any spanning forest computed by the IFT algorithm for function $f_{\max}^{\mathcal{S}_b, \mathcal{S}_o}$ or $f_{\omega}^{\mathcal{S}_b, \mathcal{S}_o}$ defines an optimum cut that maximizes E_o among all possible segmentation results satisfying the hard constraints. Any spanning forest computed by the IFT algorithm for function $f_{\max}^{\mathcal{S}_o, \mathcal{S}_b}$ or $f_{\omega}^{\mathcal{S}_o, \mathcal{S}_b}$ defines an optimum cut that maximizes E_i among all possible segmentation results satisfying the hard constraints (seeds).*

In our experiments, we used 20 real volumetric MR images of the foot in 3D. We computed the mean performance curve (Dice coefficient) for the methods: Iterative Relative Fuzzy Connectedness (IRFC), IFT with f_{\max} [10] (IFT_{FIFO}^{\max}), Power Watershed ($PW_{q=2}$), and OIFT using $f_{\max}^{\mathcal{S}_o, \mathcal{S}_b}$ ($OIFT_{inner}^{\max}$), $f_{\omega}^{\mathcal{S}_b, \mathcal{S}_o}$ ($OIFT_{outer}^{\max}$), $f_{\omega}^{\mathcal{S}_o, \mathcal{S}_b}$ ($OIFT_{inner}^{\omega}$) and $f_{\omega}^{\mathcal{S}_b, \mathcal{S}_o}$ ($OIFT_{outer}^{\omega}$) [17]. We used different seed sets obtained by eroding and dilating the ground truth (Figure 4). The experimental accuracy curves with the Sobel gradient (Figure 5) show that whenever the object presents transitions from dark to bright pixels, as it is the case with the bones talus and calcaneus, $f_{\omega}^{\mathcal{S}_o, \mathcal{S}_b}$ and $f_{\max}^{\mathcal{S}_o, \mathcal{S}_b}$ give the best accuracy results. Note also that $f_{\max}^{\mathcal{S}_b, \mathcal{S}_o}$ and $f_{\omega}^{\mathcal{S}_b, \mathcal{S}_o}$ present the worst accuracy values, by specifying the wrong orientation.

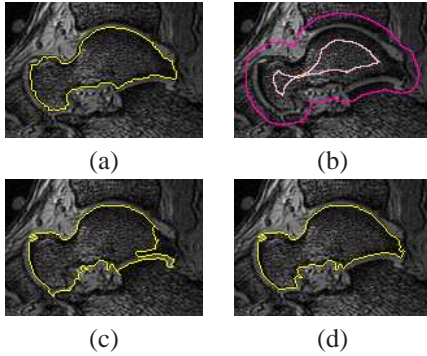


Fig. 4. (a) Ground truth of the talus in an MR image of a foot. (b) Seed sets obtained by eroding and dilating the ground truth. (c) Segmentation by IRFC. (d) An improved result by exploiting the boundary polarity using $f_{\max}^{\mathcal{S}_o, \mathcal{S}_b}$.

VI. SHAPE CONSTRAINTS VIA NSCF

Shape constraints, such as the star-convexity prior introduced by Veksler [25], can limit the search space of possible delineations to a smaller subset, thus eliminating false candidate boundaries. In this context, a point p is said to be visible to c via a set \mathcal{O} if the line segment joining p to c lies in the set \mathcal{O} . An object \mathcal{O} is star-convex with respect to center c , if every point $p \in \mathcal{O}$ is visible to c via \mathcal{O} (Figure 6). In the case of multiple stars, a computationally tractable definition, was proposed in [24], using a *Geodesic Star Convexity* (GSC) constraint in the segmentation by *min-cut/max-flow*.

In [18], we proposed an IFT extension that incorporates the GSC constraint, favoring the segmentation of objects with more regular shape, resulting in a novel method called *IFT with Geodesic Star Convexity Constraints* (GSC-IFT). In this method, the set of star centers is taken as the set of

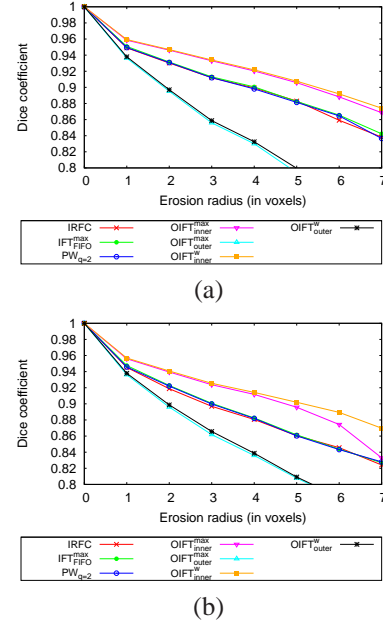


Fig. 5. The mean accuracy curves (Dice) using the Sobel gradient for the 3D segmentation of: (a) talus, and (b) calcaneus.

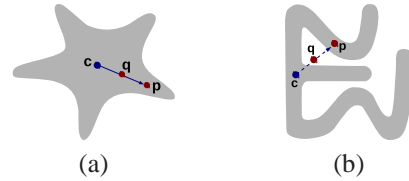


Fig. 6. For any point p within the object and the star center c , we have: (a) a star-convex object and (b) a non-star-convex object.

internal seeds (\mathcal{S}_o), and the line segments are the paths that form a spanning forest rooted at the internal seeds. The forest topology is controlled by a parameter β . For lower values of β ($\beta \approx 0.0$), the method imposes more star regularization to the boundary of the object (Figures 7 and 8), and for higher values of β , it allows a better fit to the curved protrusions and indentations of the boundary.

Thereafter, in [19] we proposed the novel method called *OIFT with Geodesic Star Convexity* (GSC-OIFT), which incorporate Gulshan’s geodesic star convexity prior in the OIFT approach for interactive image segmentation, in order to simultaneously handle boundary polarity and shape constraints (Theorem 2). This method permits the customization of the segmentation by IFT to better match the features of a particular target object (Figure 9). We constrain the search for optimum result, that maximize the graph-cut measures E_i (Eq. 2) or E_o (Eq. 3), only to segmentations that satisfy the geodesic star convexity constraint. We compute a geodesic forest P_{sum} for f_{sum} [10] by the regular IFT algorithm, using only \mathcal{S}_o as seeds, for the given digraph G , obtaining two sets of arcs $\xi_{P_{sum}}^i = \{(s, t) \in \xi \mid s = P_{sum}(t)\}$ and $\xi_{P_{sum}}^o = \{(s, t) \in \xi \mid t = P_{sum}(s)\}$. The GSC constraint is violated when $\mathcal{C}_i(L) \cap \xi_{P_{sum}}^i \neq \emptyset$ or $\mathcal{C}_o(L) \cap \xi_{P_{sum}}^o \neq \emptyset$

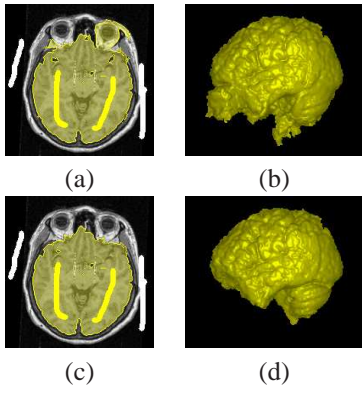


Fig. 7. Example of 3D skull stripping from user-selected markers. (a-b) Segmentation result by IFT with f_{\max} . (c-d) An improved result is obtained by exploiting the Geodesic Star Convexity (GSC-IFT with $\beta = 0.1$).

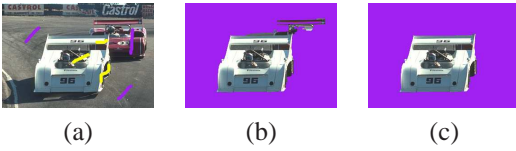


Fig. 8. (a) Input image with user-selected markers. (b) Segmentation result by IFT with f_{\max} . (c) Segmentation result by GSC-IFT ($\beta = 0.1$).

(Figure 10).

Theorem 2 (Inner/outer-cut boundary optimality). *For a given image graph $G = \langle \mathcal{V}, \xi, \omega \rangle$, consider a modified weighted graph $G' = \langle \mathcal{V}, \xi, \omega' \rangle$, with weights $\omega'(s, t) = -\infty$ for all $(s, t) \in \xi_{P_{\text{sum}}}^{\mathcal{O}}$, and $\omega'(s, t) = \omega(s, t)$ otherwise. For two given sets of seeds $\mathcal{S}_{\mathcal{O}}$ and $\mathcal{S}_{\mathcal{B}}$, the segmentation computed over G' by the IFT algorithm for function $f_{\max}^{\mathcal{S}_{\mathcal{B}}, \mathcal{S}_{\mathcal{O}}}$ defines an optimum cut in the original graph G , that maximizes $E_{\mathcal{O}}(L, G)$ among all possible segmentation results satisfying the shape constraints by the geodesic star convexity, and the seed constraints. Similarly, the segmentation computed by the IFT algorithm for function $f_{\max}^{\mathcal{S}_{\mathcal{O}}, \mathcal{S}_{\mathcal{B}}}$, over a modified graph $G' = \langle \mathcal{V}, \xi, \omega' \rangle$; with weights $\omega'(s, t) = -\infty$ for all $(s, t) \in \xi_{P_{\text{sum}}}^{\mathcal{I}}$, and $\omega'(s, t) = \omega(s, t)$ otherwise; defines an optimum cut in the original graph G , that maximizes $E_{\mathcal{I}}(L, G)$ among all possible segmentation results satisfying the shape constraints by the geodesic star convexity.*

In our experiments, we used 40 image slices of 10 thoracic CT studies to segment the liver. Figure 11a shows the mean accuracy curves for all the images assuming different seed sets obtained by eroding and dilating the ground truth. Note that for higher values of β , GSC-OIFT imposes less shape constraints, so that the accuracy tends to decrease (Figures 11b-d). Figure 12 shows some results in the case of user-selected markers.

VII. CONCLUSION AND FUTURE WORKS

The proposed extension GSC-OIFT includes the IFT with f_{\max} , OIFT and GSC-IFT as particular cases, depending on the configuration of its parameters α and β . Note that the adaptive functions presented in Section IV can't be reduced

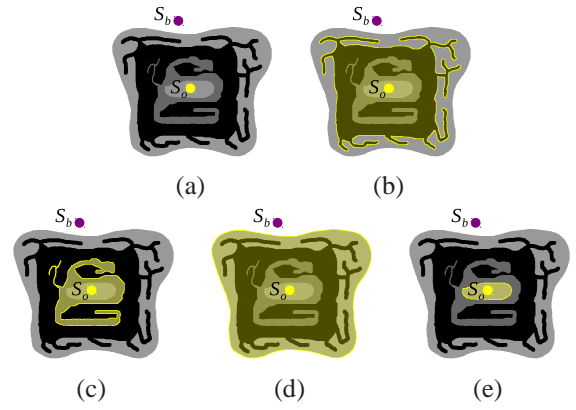


Fig. 9. (a) Synthetic image with selected markers $\mathcal{S}_{\mathcal{O}}$ and $\mathcal{S}_{\mathcal{B}}$. The target object has a regular shape with transitions from bright to dark in its border. Segmentation results by: (b) IFT obtains a non-regular shape and wrong orientation, (c) $OIFT_{\text{outer}}^{\max}$ obtains a non-regular shape, (d) GSC-IFT obtains a wrong orientation and (e) GSC- $OIFT_{\text{outer}}^{\max}$ (simultaneously considering boundary polarity and shape constraints) obtains a correct matching with the characteristics of the target object.

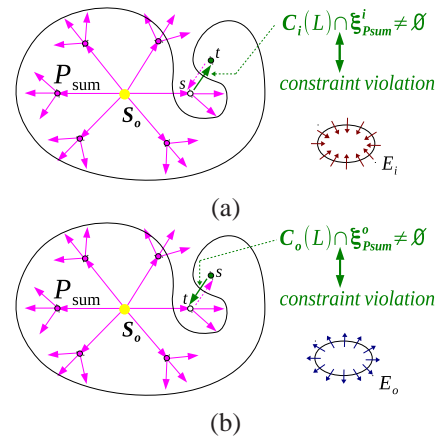


Fig. 10. The GSC constraint is violated when: (a) there is an arc $(s, t) \in \mathcal{C}_{\mathcal{I}}(L) \cap \xi_{P_{\text{sum}}}^{\mathcal{I}} \neq \emptyset$, or (b) there is an arc $(s, t) \in \mathcal{C}_{\mathcal{O}}(L) \cap \xi_{P_{\text{sum}}}^{\mathcal{O}} \neq \emptyset$.

to a GSC-OIFT computation. As a result of the theoretical foundation proposed in this work, four conference papers were published in international events of high regard [17], [18], [19], [20], and one journal paper was published in the *IEEE Transactions on Image Processing* (impact factor: 3.111) [16]. This work has also allowed new achievements that were recently published, such as [26] and [27].

As future work, we intend to combine the proposed methods with statistical models to automatically define seeds for automatic segmentation.

ACKNOWLEDGMENT

The authors thank FAPESP grant #2011/50761-2 #2012/06911-2, CNPq (305381/2012-1, 486083/2013-6), CAPES, NAP eScience - PRP - USP, FINEP project (1266/13) in biomedical engineering and Dr. J.K. Uduapa (MIPG-UPENN) for the images.

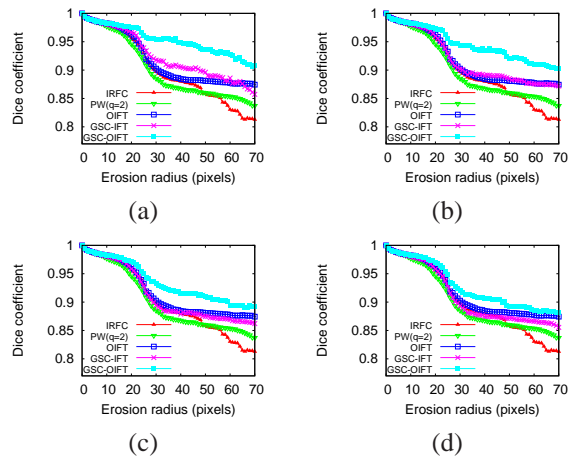


Fig. 11. The mean accuracy curves of all methods for the liver segmentation for various values of β : (a) $\beta = 0.0$, (b) $\beta = 0.2$, (c) $\beta = 0.5$, and (d) $\beta = 0.7$.

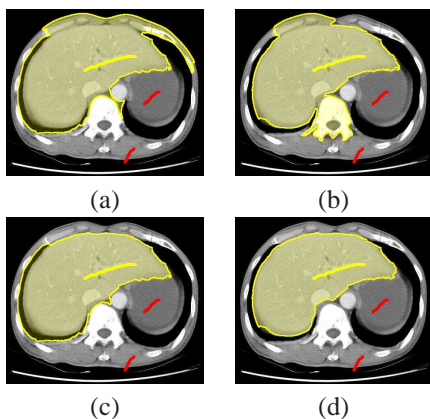


Fig. 12. Results for user-selected markers: (a) IRFC, (b) OIFT ($J_{\max}^{S_b, S_o}$ with $\alpha = 0.5$), (c) GSC-IFT ($\beta = 0.7$), and (d) GSC-OIFT ($\beta = 0.7$, $\alpha = 0.5$).

REFERENCES

- [1] L. Mansilla, "Image foresting transform with non-smooth connectivity functions: Adaptive weights, boundary polarity, and shape constraints," Master's thesis, Institute of Mathematics and Statistics, University of São Paulo, Brazil, Feb 2014. [Online]. Available: <http://www.teses.usp.br/teses/disponiveis/45/45134/tde-17032014-121734/pt-br.php>
- [2] M. Sonka, R. Boyle, and V. Hlavac, *Image Processing, Analysis and Machine Vision*. ITP, 1999.
- [3] A. Madabhushi and J. Udupa, "Interplay between intensity standardization and inhomogeneity correction in mr image processing," *IEEE TMI*, vol. 24, no. 5, pp. 561–576, 2005.
- [4] X. Bai and G.apiro, "Distance cut: interactive segmentation and matting of images and videos," in *IEEE International Conference on Image Processing (ICIP)*, vol. 2, San Antonio, Texas, 2007, pp. II – 249–II – 252.
- [5] A. Falcão, J. Udupa, S. Samarasekera, S. Sharma, B. Hirsch, and R. Lotufo, "User-steered image segmentation paradigms: Live-wire and live-lane," *Graphical Models and Image Processing*, vol. 60, no. 4, pp. 233–260, Jul 1998.
- [6] Y. Boykov and G. Funka-Lea, "Graph cuts and efficient N-D image segmentation," *International Journal of Computer Vision*, vol. 70, no. 2, pp. 109–131, 2006.
- [7] J. Cousty, G. Bertrand, L. Najman, and M. Couprie, "Watershed cuts: Thinnings, shortest path forests, and topological watersheds," *IEEE*

- Transactions on Pattern Analysis and Machine Intelligence*, vol. 32, pp. 925–939, 2010.
- [8] L. Grady, "Random walks for image segmentation," *IEEE Transactions on Pattern Analysis and Machine Intelligence*, vol. 28, no. 11, pp. 1768–1783, 2006.
- [9] K. Ciesielski, J. Udupa, P. Saha, and Y. Zhuge, "Iterative relative fuzzy connectedness for multiple objects with multiple seeds," *Computer Vision and Image Understanding*, vol. 107, no. 3, pp. 160–182, 2007.
- [10] A. Falcão, J. Stolfi, and R. Lotufo, "The image foresting transform: Theory, algorithms, and applications," *IEEE Transactions on Pattern Analysis and Machine Intelligence*, vol. 26, no. 1, pp. 19–29, 2004.
- [11] V. Vezhnevets and V. Konouchine, "'growcut' - interactive multi-label N-D image segmentation by cellular automata," in *Proc. Graphicon*, 2005, pp. 150–156.
- [12] P. Miranda and A. Falcão, "Elucidating the relations among seeded image segmentation methods and their possible extensions," in *XXIV Conference on Graphics, Patterns and Images (SIBGRAPI)*. Maceió, AL: Los Alamitos: IEEE Computer Society, Aug 2011.
- [13] K. Ciesielski, J. Udupa, A. Falcão, and P. Miranda, "A unifying graph-cut image segmentation framework: algorithms it encompasses and equivalences among them," in *Proceedings of SPIE on Medical Imaging*, vol. 8314, San Diego, California, USA, 2012.
- [14] C. Couprie, L. Grady, L. Najman, and H. Talbot, "Power watersheds: A unifying graph-based optimization framework," *Transactions on Pattern Analysis and Machine Intelligence*, vol. 99, 2010.
- [15] P. Miranda, A. Falcão, and J. Udupa, "Synergistic arc-weight estimation for interactive image segmentation using graphs," *Computer Vision and Image Understanding*, vol. 114, no. 1, pp. 85–99, 2010.
- [16] P. Miranda and L. Mansilla, "Oriented image foresting transform segmentation by seed competition," *IEEE Transactions on Image Processing*, vol. 23, no. 1, pp. 389–398, Jan 2014.
- [17] L. Mansilla and P. Miranda, "Image segmentation by oriented image foresting transform: Handling ties and colored images," in *18th International Conference on Digital Signal Processing (DSP)*. Santorini, Greece: IEEE, Jul 2013, pp. 1–6.
- [18] L. Mansilla, M. Jackowski, and P. Miranda, "Image foresting transform with geodesic star convexity for interactive image segmentation," in *IEEE International Conference on Image Processing (ICIP)*, Melbourne, Australia, Sep 2013, pp. 4054–4058.
- [19] L. Mansilla and P. Miranda, "Image segmentation by oriented image foresting transform with geodesic star convexity," in *Computer Analysis of Images and Patterns (CAIP)*, vol. 8047, York, UK, Aug 2013, pp. 572–579.
- [20] L. Mansilla, F. Cappabianco, and P. Miranda, "Image segmentation by image foresting transform with non-smooth connectivity functions," in *XXVI Conference on Graphics, Patterns and Images (SIBGRAPI)*. Arequipa, Perú: IEEE, Aug 2013, pp. 147–154.
- [21] A. Falcão, F. Bergo, F. Favretto, G. Ruppert, P. Miranda, and F. Cappabianco, *Neurociências e epilepsia. Capítulo: Processamento, Visualização e Análise de Imagens Anatômicas do Cérebro Humano*. Plêiade, 2008, vol. 1, série CInAPCe.
- [22] P. Miranda, A. Falcão, and J. Udupa, "Cloud bank: A multiple clouds model and its use in MR brain image segmentation," in *Proceedings of the IEEE International Symposium on Biomedical Imaging (ISBI)*, Boston, MA, 2009, pp. 506–509.
- [23] F. Cappabianco, P. Miranda, J. Ide, C. Yasuda, and A. Falcão, "Unraveling the compromise between skull stripping and inhomogeneity correction in 3T MR images," in *Conference on Graphics, Patterns and Images (SIBGRAPI 2012)*, Aug 2012, pp. 1–8.
- [24] V. Gulshan, C. Rother, A. Criminisi, A. Blake, and A. Zisserman, "Geodesic star convexity for interactive image segmentation," in *Proceedings of Computer Vision and Pattern Recognition*, 2010, pp. 3129–3136.
- [25] O. Veksler, "Star shape prior for graph-cut image segmentation," in *European Conference on Computer Vision (ECCV)*, vol. 5304, 2008, pp. 454–467.
- [26] C. Braz and P. Miranda, "Image segmentation by image foresting transform with geodesic band constraints," in *IEEE International Conference on Image Processing (ICIP)*, Paris, France, Oct 2014, pp. 4333 – 4337.
- [27] H. Bejar and P. Miranda, "Oriented relative fuzzy connectedness: Theory, algorithms, and applications in image segmentation," in *XXVII Conference on Graphics, Patterns and Images (SIBGRAPI)*. Rio de Janeiro, Brazil: IEEE, Aug 2014, pp. 304–311.